Structural and Multidisciplinary Optimization manuscript No.
(will be inserted by the editor)

M.A. Luersen · R. Le Riche · D. Lemosse · O. Le Maître

A computationally efficient approach to swimming monofin optimization

Received: date / Revised: date

Abstract Monofins provide swimmers with an efficient alternative to the standard pair of fins. For example, all short and long distance human swimming records have been established using monofins. Current monofin design is mostly empirical, so the objectives of this work are to analyze monofin propulsion through coupled fluid-structure simulation and to optimize its flexural stiffness distribution. The optimization process maximizes the propulsive power provided by the monofin with a constraint on the total expended power. In order to be able to carry out the optimization of the coupled fluid-structure system which is numerically costly to evaluate, the following simplifications are proposed: (i) a two-dimensional unsteady, inviscid and incompressible fluid flow is considered; (ii) the swimmer is composed of linear articulated segments, whose kinematics is imposed and identified from experimental data; (iii) the monofin is represented by rigid bars linked by torsional springs. For various allowable swimmer powers optimal 2D stiffness distributions are obtained using the Globalized and Bounded Nelder-Mead algorithm. Finally, an identification procedure is described to translate the optimal 2D stiffness distributions into 3D thickness profiles for a given monofin planform shape.

M.A. Luersen
DAMEC - Departamento de Mecânica - CEFET-PR
Av. Sete de Setembro, 3165
80230-901 - Curitiba - PR - Brazil
E-mail: luersen@cefetpr.br

R. Le Riche
Ecole des Mines de Saint Etienne, 158 cours Fauriel
42023 - Saint Etienne cedex 2 - France
E-mail: leriche@emse.fr

D. Lemosse
LMR - Laboratoire de Mécanique de Rouen - INSA de Rouen
Avenue de l'Université
76801 - Saint Etienne du Rouvray - France
E-mail: Didier.Lemosse@insa-rouen.fr

O. Le Maître
Laboratoire de Mécanique et d'Energétique d'Evry
Université d'Evry Val d'Essonne, 40 rue du Pelvoux
91020 - Evry - France
E-mail: Olivier.Lemaitre@iup.univ-evry.fr

Keywords Monofin Design · Swimming Propulsion · Identification · Optimization

1 Introduction

Monofins already provide the most efficient way of swimming for human beings. However, it is expected that further progress can be achieved because today's monofin design is empirical and studies in aquatic locomotion modes and oscillating hydrofoils show that more efficient swimming systems exist. Fish like tuna, mackerel, sharks and marine mammals have propulsive efficiencies greater than 90% at high swimming speed in calm waters (Sfakiotakis et al (1999)). Similar efficiencies have been observed for artificial oscillating hydrofoils (Pedro et al (2003); Anderson et al (1998)). Previous works have been devoted to describing the physics and physiology of fin-swimming (Zamparo et al (2002); Baly et al (2001)). The objective of the current work is to propose a rationale for designing monofins.

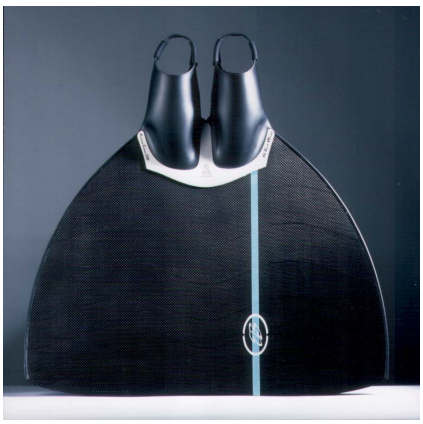

Fig. 1 Carbon monofin (Breier©).

The simulation of the swimmer and monofin system is very complex: the flow is unsteady, it interacts with the fin

which is a composite structure in dynamic motion with large displacements. There are many works related to the fluid-structure interaction and its impact on structural design (e.g., Kvamsdal et al (1999)), but the numerical costs of typical fluid-structure models do not allow their optimization which requires a large number of evaluations.

In order to carry out the monofin optimization, some model simplifications are made in the first part of the article: (i) a two-dimensional unsteady, inviscid and incompressible fluid flow without separation is assumed; (ii) the swimmer is represented by linear articulated segments whose kinematics is identified from experimental swimmer data and imposed; (iii) the monofin is represented by rigid bars linked by torsional springs with large rotations allowed. Due to the small monofin thickness and flow features, the sheet vortex fluid model presented in Le Maître et al (1999) is used.

In the second part of the article, the propulsive power provided by the monofin is maximized with a constraint on the maximum total power expended by the swimmer. The design variables are the spring rigidities. The optimization problem is solved by the Globalized and Bounded Nelder-Mead (GBNM) algorithm (Luersen et al (2004)).

The two-dimensional swimmer-fin model was firstly introduced in Luersen et al (2003). Also, some preliminary optimization results of the 2D system were given in this reference.

The flexural stiffness distribution obtained from the two-dimensional optimization is finally translated into a three-dimensional monofin (cf. Fig. 1). The mapping can be seen as an identification procedure where the "experience" is a 2D bars system whose behavior is approximated by a 3D finite element model of the fin. The equivalence between the two models can be sought in terms of static behavior, dynamic behavior, or a mix of static and dynamic behaviors. The advantages of static equivalence is that the load cases can be taken from the 2D flow simulation and large displacements analyses are available. However, it neglects the fin inertia. On the contrary, the modal dynamic identification accounts for both flexural and inertial terms but it is, in essence, a small displacements analysis. The 3D thickness distribution is found by minimizing an error function between the static and/or modal response of the 2D and 3D monofins. The GBNM minimization algorithm carries out the identifications.

2 Two-dimensional modelling of the system

A two-dimensional model of the swimmer-fin system is proposed which is based on the following assumptions. The Reynolds number for the system is of the order of 10^6, so the viscosity is neglected. By further neglecting obstacles thickness, flow separation and water compressibility, the unsteady vortex based flow model of Le Maître et al (1999) can be used: the velocity field is obtained by the superposition of a uniform fluid flow and a field induced by vortices emitted at the finÂ´s trailing edge. The vortex intensities are calculated at each instant so that the following hold: (i) the flow remains attached along the obstacle; (ii) the flows from the upper and the lower surfaces join smoothly at the trailing edge (Kutta condition); (iii) the total circulation is constant. The advantage is that only the solid boundary and the wake are discretized, as opposed to meshing the whole domain, so that computer time is saved.

The swimmer is represented by 4 segments: the arms, the torso, the thighs and the tibias. The monofin is modelled by 6 rigid bars articulated by torsional springs with large rotations allowed (Fig. 2). All bars have equal and constant linear mass density. From the analysis of a monofin swimmer video the swimmer movement is approximately segment-wise harmonic:

$$y_1(t) = Y_1^c + Y_1 \sin(2\pi f t) \,, \tag{1}$$

$$\theta_i(t) = \Theta_i^c + \Theta_i \sin(2\pi f t - \phi_i) \,, \tag{2}$$

where y_1 is the vertical displacement of the hand, θ_1 is the slope between the horizontal and the arms, ϕ_1 is the phase angle between the vertical hand movement and the arm rotation, θ_i and ϕ_i, $i = 2,5$ are the angles and the phases between the segments $(i-1)$ and i, respectively. The parameters of Eqs. (1) and (2) (the amplitudes Y_1 and Θ_i, the mean values Y_1^c and Θ_i^c, the phase angles ϕ_i and the frequency f) and the mean swimmer speed (considered to be the free-stream speed) U_∞ are identified from measured vertical displacements of the hand, neck, shoulder, elbow, hip, knee, ankle and toe of a sprint swimmer. The following values are obtained (Luersen et al (2003)): $U_\infty = 3.0\ m/s$, $Y_1 = 0.07\ m$, $Y_1^c = 0.0\ m$, $\Theta_1 = 3.4^\circ$, $\Theta_1^c = -1.6^\circ$, $\phi_1 = -222.6^\circ$, $\Theta_2 = 12.0^\circ$, $\Theta_2^c = 1.6^\circ$, $\phi_2 = -152.8^\circ$, $\Theta_3 = 20.0^\circ$, $\Theta_3^c = -10^\circ$, $\phi_3 = 17.2^\circ$, $\Theta_4 = 14.0^\circ$, $\Theta_4^c = 14.0^\circ$, $\phi_4 = 17.2^\circ$, $\Theta_5 = 16.0^\circ$, $\Theta_5^c = -20.0^\circ$ and $\phi_5 = 107.2^\circ$.

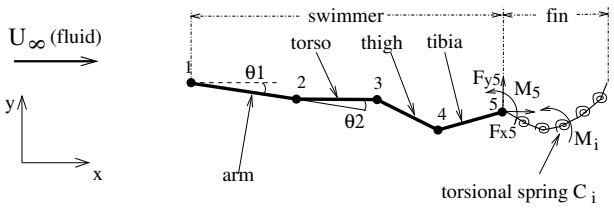

Fig. 2 Swimmer and monofin representation.

The displacements of the first monofin bar ($\theta_5(t)$, $x_5(t)$ and $y_5(t)$) are imposed because they follow the feet. The forces distributed over the fin are obtained by means of a coupled fluid-structure calculation. The unknowns of the problem are the orientations, the angular velocities and the angular accelerations of the monofin's bar joints ($\theta_i(t)$, $\dot{\theta}_i(t)$, $\ddot{\theta}_i(t)$, $i = 6,10$), and the efforts at the point 5 (which is approximately the swimmer's ankle), $F_{x5}(t)$, $F_{y5}(t)$, $M_5(t)$. The monofin dynamic equilibrium equations are solved by the Newmark time integration scheme (Géradin and Cardona (2001)). At each iteration, the system of non-linear equations is solved using a mixed Newton-Raphson/GBNM scheme.

The GBNM algorithm (see paragraph 4.2 and Luersen et al (2004)) is employed to minimize the residue of the equations when the Newton-Raphson iterations have not decreased the residue. A visualization of the flow, swimmer and monofin is given in Fig. 3.

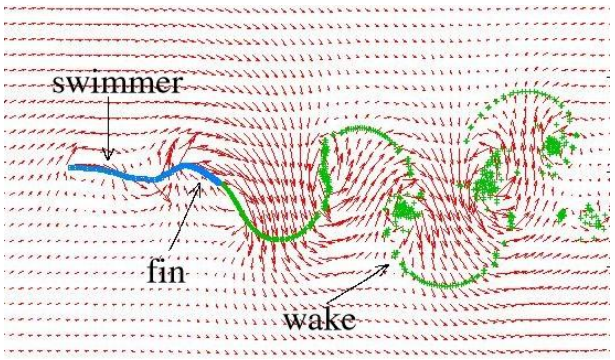

Fig. 3 Flow, swimmer and monofin visualization. Continuous trace, the obstacle; ×, the wake particles; →, the relative velocity of the fluid.

3 Optimization problem formulation

As the majority of the thrust is produced by the monofin, the purpose of the optimization is to maximize the propulsive power provided by the monofin with a constraint on the maximum total power expended by the swimmer at the fin. The time-averaged propulsive power is defined as,

$$\bar{P}_{fx} = \frac{1}{T_f - T_s} \int_{T_s}^{T_f} \int_0^{L_s} f_x(s) |U_\infty| \, ds \, dt \, , \tag{3}$$

and the time-averaged power supplied by the fluid to the fin is,

$$\bar{P}_f = \frac{1}{T_f - T_s} \int_{T_s}^{T_f} \int_0^{L_s} (f_x(s)(\dot{x}(s) + |U_\infty|) + f_y(s)\dot{y}(s)) \, ds \, dt \, , \tag{4}$$

where U_∞ is the swimmer's mean forward speed, $\dot{x}$ and $\dot{y}$ are the velocity components of the fin in a stationary reference system with respect to the fluid speed U_∞, $f_x(s)$ and $f_y(s)$ are the fluid forces per unit length over the fin at the fin natural coordinate s, L_s is the monofin's length, T_s and T_f are the starting and final calculation times. Energy transmissions on the swimmer's body are neglected in comparison with the fin, consequently $\bar{P}_f$ is considered to be the power provided to the swimmer. For a swimmer going up-stream, $\bar{P}_{fx}$ and $\bar{P}_f$, calculated by Eqs. (3) and (4), are negative. Thus, the objective function to be minimized is $\bar{P}_{fx}$ with a lower bound on the total power $\bar{P}_f$. The design variables are the torsional stiffnesses C_i. The optimization problem is formulated as,

$$\begin{cases} \min\limits_{C_i} \bar{P}_{fx} \, , \\ \text{such that,} \\ \bar{P}^{min} \leq \bar{P}_f \, , \\ C_i^{min} \leq C_i \leq C_i^{max} \, , \quad i = 1,5 \, . \end{cases} \tag{5}$$

Table 1 Effects of varying the monofin's length L_s on the power balance.

L_s (m)	0.5	0.72	1.0
$\bar{P}_{fx}$ (W)	−527.62	−809.67	−1147.28
$\bar{P}_f$ (W)	−1153.30	−1369.88	−1747.60
ν_P	0.457	0.591	0.656

Table 2 Effects of changing all stiffness values on the power balance.

C_i, $i=1,5$ (Nm/rad)	300	500	1000	5000	10000	15000
$\bar{P}_{fx}$ (W)	−780.38	−749.39	−809.67	−1052.15	−952.02	−846.08
$\bar{P}_f$ (W)	−950.34	−1008.32	−1369.88	−3917.57	−4955.79	−5270.33
ν_P	0.821	0.743	0.591	0.269	0.192	0.161

4 Stiffness optimization results and discussion

4.1 Parametric studies

In order to have an intuitive comprehension of the system behavior, parametric studies are now described where the monofin's length and spring stiffnesses change. In the first study, the monofin's length L_s varies, while rigidities are fixed at $C_i = 1000 \; Nm/rad$. Table 1 presents the effects on $\bar{P}_{fx}$, $\bar{P}_f$, and the power efficiency $\nu_P = \bar{P}_{fx}/\bar{P}_f$. Increasing L_s improves $\bar{P}_{fx}$ and ν_P, at the expense of a higher $\bar{P}_f$. From now on, the monofin's length is set to 0.72 m, which is the length of the monofin used by the swimmer whose kinematics was identified.

Tables 2 and 3 summarize the effect of the rigidities C_i on $\bar{P}_{fx}$, $\bar{P}_f$ and ν_P. In Table 2, all the stiffnesses are changed together. In Table 3, a reference case where $C_i = 1000 \; Nm/rad$, $i = 1,5$, is perturbed by setting one of the C_i to $2000 \; Nm/rad$.

From these studies, the following pieces of information are obtained:

- Higher fin stiffness implies more power expended by the swimmer. The effect on propulsive power is not monotonous: $\bar{P}_{fx}$ first increases and then decreases with C_i;
- Moving the higher stiffness near the leading edge increases both $\bar{P}_{fx}$ and $\bar{P}_f$ while it decreases ν_P;
- The efficiency ν_P is higher for lower fin stiffnesses;
- The propulsive power $\bar{P}_{fx}$ and the total power $\bar{P}_f$ are more sensitive to spring stiffnesses near the fin's leading edge than near the trailing edge.

Table 3 Effects of changing one spring stiffness.

C_1	1000	**2000**	1000	1000	1000	1000
C_2	1000	1000	**2000**	1000	1000	1000
C_3	1000	1000	1000	**2000**	1000	1000
C_4	1000	1000	1000	1000	**2000**	1000
C_5	1000	1000	1000	1000	1000	**2000**
$\bar{P}_{fx}\ (W)$	−809.67	−927.97	−832.36	−789.65	−790.545	−804.12
$\bar{P}_f\ (W)$	−1369.88	−1748.94	−1512.46	−1382.90	−1354.35	−1362.15
v_P	0.591	0.531	0.550	0.571	0.584	0.590

4.2 Optimization

The optimization problem (Eq. (5)) is solved by means of the Globalized and Bounded Nelder-Mead algorithm (Luersen et al (2004)). The GBNM is a local-global optimization method based on probabilistic restart. Local searches are performed by an improved Nelder-Mead algorithm (Nelder and Mead (1965)) where design variables are continuous and can be bounded, inequality constraints are taken into account by adaptive penalization, and some search failure cases (e.g. simplex degeneracy) prevented. The GBNM does not need gradient calculation.

The optimization problem is solved for three limits on the swimmer's total power, $\bar{P}^{min} = -1400$, -2000 and $-3000\ W$. As a comparison, the power measured on average distance swimmers in di Prampero et al (1974) was about 1400 W. The higher limits in the second and third cases account for the shorter distance and the 2D model that overestimates efforts (the fluid cannot go around the sides of the obstacle and there is no flow separation). The fin rigidities are bounded by: $C_i^{min} = 300\ Nm/rad$ and $C_i^{max} = 15000\ Nm/rad$, $i = 1,5$. Figure 4 shows the stiffness distributions for each optimization problem and Table 4 presents the associated power balances. The optimal stiffness distributions are tapered from the leading to the trailing edge. Changes in swimmer total power affect mainly the fin near the leading edge while low stiffness are always optimal near the trailing edge. As will be seen in the final monofin design (Section 6), this optimization result suggests an increased flexural stiffness near the leading edge. Figure 5 shows the vertical positions of the fin's leading and trailing edges as a function of time for the optimal monofin when $P^{min} = -2000\ W$.

Table 4 Power balances for optimal stiffness distributions.

$\bar{P}^{min}\ (W)$	−1400	−2000	−3000
$\bar{P}_{fx}\ (W)$	−973.15	−1129.01	−1208.37
$\bar{P}_f\ (W)$	−1399.99	−1999.54	−2988.16
v_P	0.695	0.565	0.404

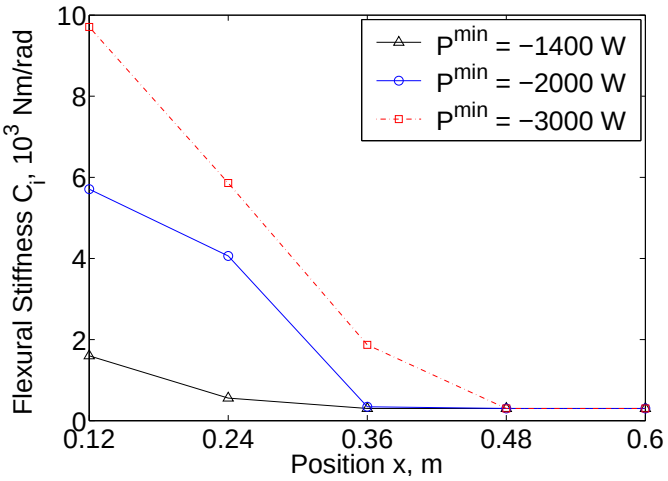

Fig. 4 Optimal stiffness distributions.

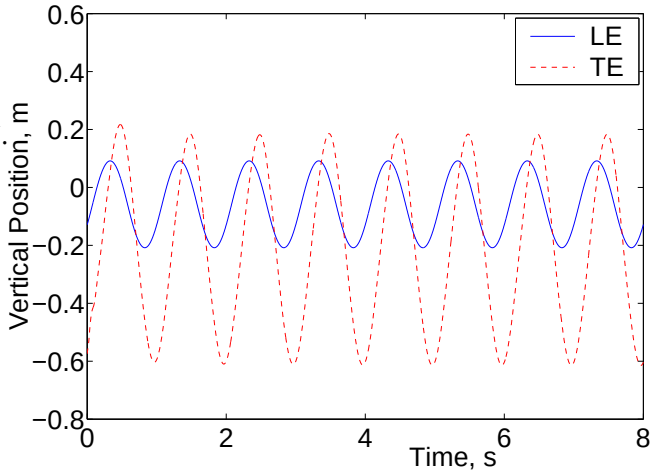

Fig. 5 Evolution of the vertical positions of the fin's leading and trailing edges (LE and TE) for the optimal monofin under the constraint $P^{min} = -2000\ W$.

5 Translation into a 3D structure

The stiffness distribution obtained from the previous two-dimensional optimization is now translated into a three-dimensional structure. The mapping can be seen as an identification procedure where the "experience" is a 2D bars system whose behavior is approximated by a 3D finite element model of the fin. In its most general statement, this identification problem is ill-posed since the 3D system has more degrees of freedom than its 2D counterpart. Many combinations of shape and thickness distribution can represent the 2D monofin. In practice, however, the planform shape of the monofin is dic-

tated by manufacturing (cost of molds) and marketing considerations which has yielded forms that mimmick marine mammals (cf. Fig. 1). Once the fin planform shape is given, the spring stiffnesses can be mapped into a fin thickness distribution. Because the fin is manufactured using composite prepreg layup, the thickness is kept constant spanwise and varies chordwise at ply drops. The equivalence between the two models can be sought in terms of static behavior, modal behavior, or a mix of static and modal behaviors. The advantages of the static equivalence is that large displacements analyses may be available. However, it neglects the fin inertia in comparison to water inertia and fin flexural stiffness. On the contrary, the modal dynamic identification accounts for both fin inertia and flexural stiffness but it is, in essence, a small displacements analysis. Furthermore, 3D non-bending modes have no pendant in the 2D system, and higher natural bending frequencies are far away from the frequency of the imposed movement. Hence, the first natural bending mode is more relevant than other natural bending modes. For these reasons, only the first natural mode, which has empirically been found on the monofin to consistently be bending, is considered. The 3D thickness distribution is found by minimizing

$$J = \alpha J_{static} + (1-\alpha) J_{freq} \ , \tag{6}$$

where,

$$J_{static} = \frac{\sum_{i=1}^{NCP} ((u_i-\tilde{u}_i)^2+(v_i-\tilde{v}_i)^2)}{\sum_{i=1}^{NCP} (u_i^2+v_i^2)} \quad \text{and} \quad J_{freq} = \frac{|w_1^2-\tilde{w}_1^2|}{w_1^2} \ . \tag{7}$$

α is a weight factor between 0 and 1, that balances contributions from static and modal criteria, (u_i, v_i) are the target displacements at the bar joints of the simplified model, $(\tilde{u}_i, \tilde{v}_i)$ are the displacements at the *NCP* corresponding control points of the 3D finite element model, w_1 is the target first natural circular frequency of the simplified model and $\tilde{w}_1$ is the first natural circular frequency of the finite element model.

The 3D fin is analyzed with a finite element model which relies on solid elements improved for thin structures (Lemosse and Dhatt (2000)). The parameterization of the fin is described in Fig. 6.

The final thickness distribution is identified by solving,

$$\begin{cases} \min\limits_{h_i} J \ , \\ \text{such that,} \\ h_i^{min} \ \leq \ h_i \ \leq \ h_i^{max} \ , \quad i = 1,6 \text{ and} \\ h_i \ \leq \ h_{i-1} \ , \quad i = 2,6 \end{cases} \tag{8}$$

where the thicknesses h_i are bounded by $h_i^{min} = 1.5 \times 10^{-4}\ m$ and $h_i^{max} = 2 \times 10^{-2}\ m$, $i = 1,6$. The constraints $h_i \ \leq \ h_{i-1}$, $i = 2,6$, are handled by reordering the variables h_i in the finite element (FE) analysis but keeping them unordered in the optimization. It was observed on the current problem that this reordering is more efficient than the adaptive penalization of the GBNM optimizer.

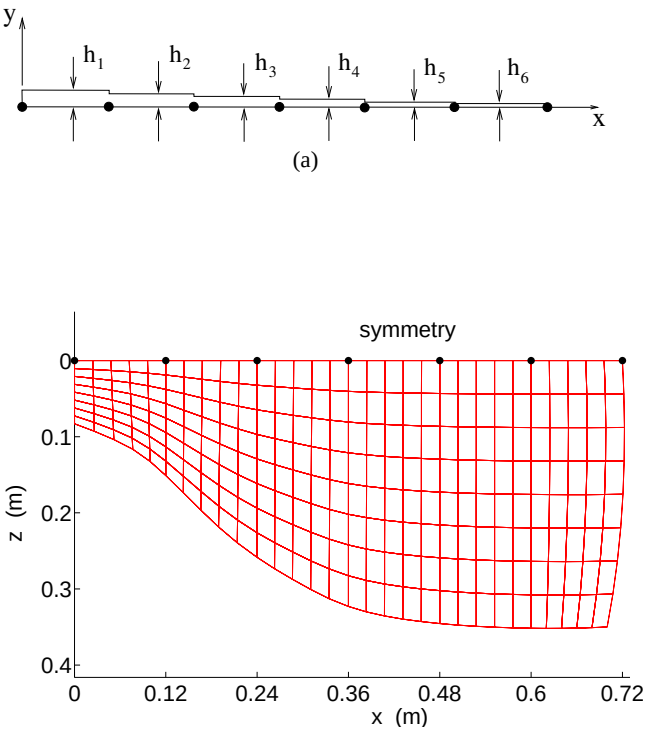

Fig. 6 Fin parameterization: thickness profile (a), half-planform shape and finite element mesh (b). The dots represent the *NCP* points where J_{static} is evaluated.

6 Identification results and discussion

Firstly, when $J = J_{static}$ ($\alpha = 1$), the influence of the load cases and the small or large displacements analyses are described. Three different vertical load cases are tested, as sketched in Fig. 7. It should be noted that there are two necessary conditions for $h^* = \arg\min J_{static}$ to be unique: 1) the equilibrium relative angles should be non-null (see Appendix A); 2) there should be at least as many control points, *NCP*, as there are design variables (6 here), otherwise many combinations of design variables may produce the same displacements at the control points.

Secondly, the difference between minimizing J_{static} and J_{freq} is exhibited.

Finally, the problem is solved for a mixed static and modal criterion ($\alpha = 0.5$).

The GBNM algorithm is used to solve problem (8). In order to protect the final design found in this work, a material description is intentionally left out and the ply thicknesses are normalized.

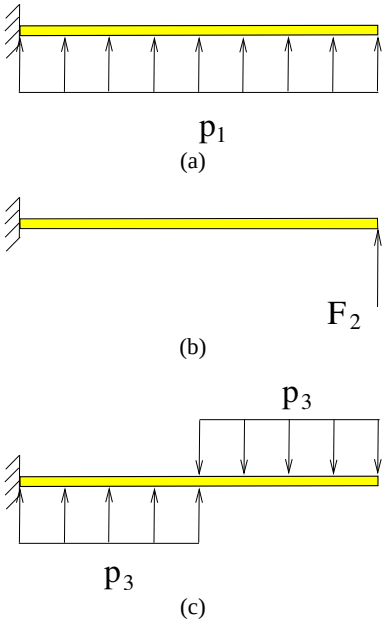

Fig. 7 The load cases considered for the thickness identification.

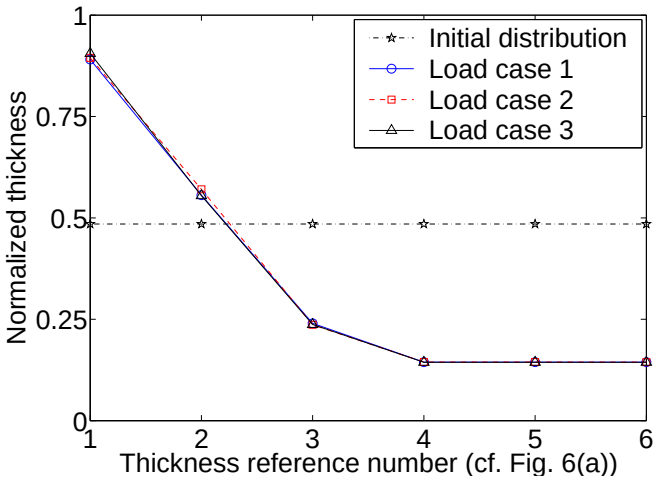

Fig. 8 Normalized identified thickness distributions for small displacements formulation.

6.1 Static small displacements formulation

First, a static analysis procedure ($\alpha = 1$ in Eq. 6) under small displacements is carried out. The three load cases of Fig. 7 are tested setting $p_1 = 4.0875\ N/m$, $F_2 = 0.73575\ N$ and $p_3 = 4.0875\ N/m$. The identified thicknesses obtained for this formulation are presented in Fig. 8. For the load cases considered, it can be noted that the thickness distributions are very close, the main difference being a 2.5% variation in h_2 value. Figure 9 shows the deformed positions of the simplified 2D bars model and the mid-plane symmetry line ($z = 0$) of the FE model built using the thicknesses identified under load case 1.

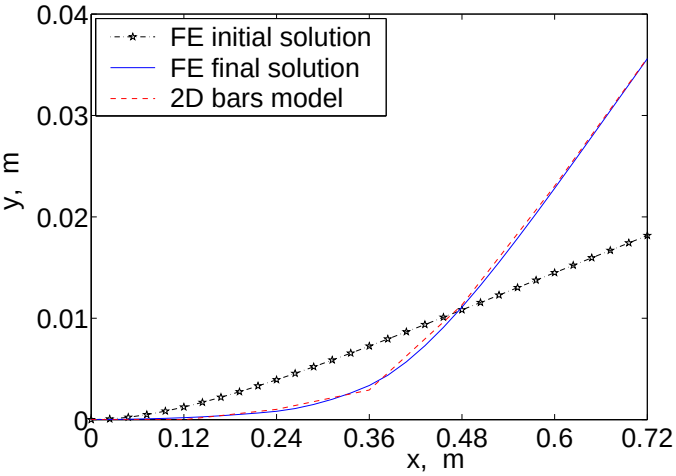

Fig. 9 Deformed shapes comparison for small displacements formulation, load case 1.

6.2 Static large displacements formulation

The three load distributions used in the small displacements identification are kept but the intensities are six times higher in order to generate a large displacements problem: $p_1 = 24.525\ N/m$, $F_2 = 4.4145\ N$ and $p_3 = 24.525\ N/m$.

The identified thicknesses are presented in Fig. 10. For the load cases considered, it can be noted that thickness distributions are close, the main difference being a 9% variation in the h_2 value. Figure 11 shows the deformed shape of the bars model and the mid-plane symmetry line ($z = 0$) of the FE model built using the identified thicknesses under load case 1.

Table 5 shows the first natural frequency of the 3D fin for static formulation solutions. The reader should keep in mind that frequencies are not accounted for in the static identifications. The difference in $\tilde{f}_1$ is less than 0.5% and 1.8% among small and large displacements solutions, respectively. For all static formulations it is less than 3.5%.

It is observed that for the static small displacements formulation the load case influence is very small. For the large displacements procedure there is a higher difference among the results obtained with different load cases. Probably because in a large displacements (geometrically non-linear) FE analysis the displacements are stress dependent, and different load cases generate different state of stresses. The solutions in small and large displacements are close, with large displacements solutions being thicker near the monofin's leading edge (see Fig. 13). This is explained by the fact that

Table 5 First natural frequency ($\tilde{f}_1 = \frac{\tilde{w}_1}{2\pi}$), in *hz*, for static formulation solutions.

Load case	Small displacements	Large Displacements
1	2.4842	2.5584
2	2.4777	2.5137
3	2.4720	2.5208

large displacements analysis generates larger vertical displacements in the clamped region.

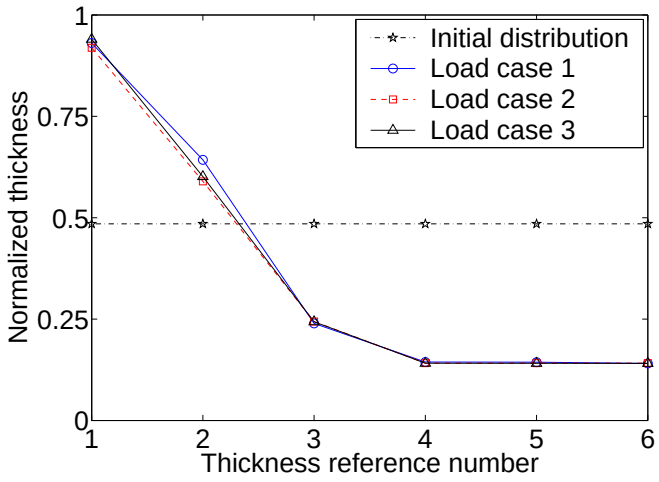

Fig. 10 Normalized identified thickness distributions for large displacements formulation.

6.3 First natural frequency formulation

In this identification procedure, only the first natural frequency is considered ($\alpha = 0$ in Eq. 6). The first natural frequency of the 2D system is $f_1 = \frac{w_1}{2\pi} = 1.5400$ *hz*. It was numerically observed that this formulation presents many solutions that are very close, i.e., many thickness distributions correspond to the frequency f_1. Figure 12 shows the solutions found by GBNM optimization algorithm having a deviation smaller than 1×10^{-4} *hz*, and the corresponding modes, in a single run of 1500 analyses. Note that the GBNM algorithm has a restart procedure which permits to locate different local optima in a single run.

There are several solutions going from highly tapered to uniform thickness. The maximum amplitude is at trailing edge for all solutions. The maximum curvature changes, moving from the clamped region for Solution 1, towards the trailing edge for Solutions 2 and 3, respectively.

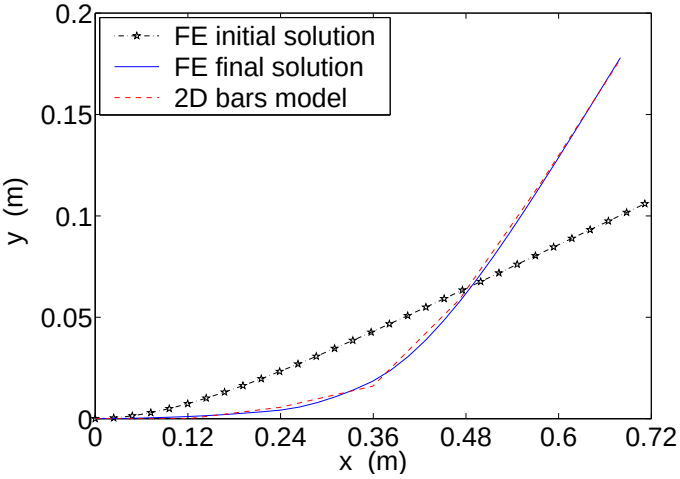

Fig. 11 Deformed shapes comparison for large displacements formulation, load case 1.

6.4 Mixed formulation

In order to take into account both static and dynamic behaviors of the monofin, a mixed criterion ($\alpha = 0.5$ in Eq. 6) is used. For the static analysis, only load case 1 under small displacements is considered since load cases do not generate different solutions (at the condition that the equilibrium angles are non-null, cf. Appendix A), and the discrepancies between large and small displacements solutions are negligible.

Figure 13 compares solutions to the mixed, the static linear (small displacements and $\alpha = 1$), and the static nonlinear (large displacements and $\alpha = 1$) problems. Figure 14 shows the deformed shapes of the bars model and the midplane symmetry line ($z = 0$) of the FE model built with the identified thicknesses. For the mixed formulation solution, the first natural frequency of the finite element model is $\tilde{f}_1 = \frac{\tilde{w}_1}{2\pi} = 2.2115$ *hz*.

In comparison to the static analysis formulations, material is removed from the clamped region and added at the tip. This provides lower first natural frequency, which is closer to the 2D model. This is traded against a slight departure from the targetted static deformed shape.

As can be seen in Fig. 13, every optimized profile advocates an increased thickness near the leading edge and a thinner trailing edge area, in comparison to a state of the art design (a commercialized Breier's monofin).

7 Conclusion

A strategy for optimizing a swimming monofin has been presented. It is based on the optimization of a simplified two-dimensional swimmer-fin-fluid model followed by a map-

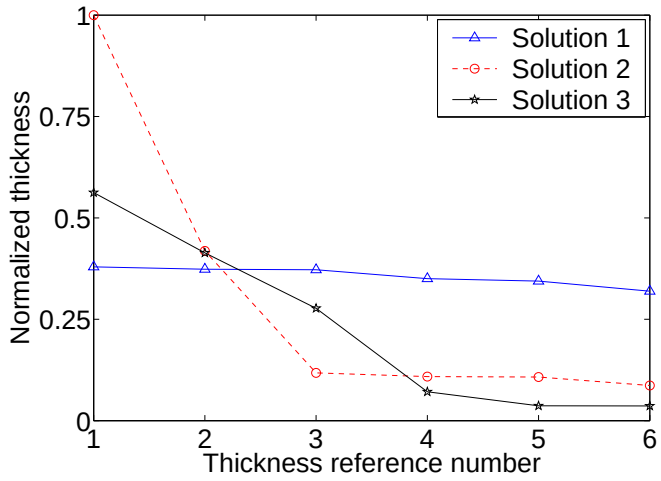

(a)

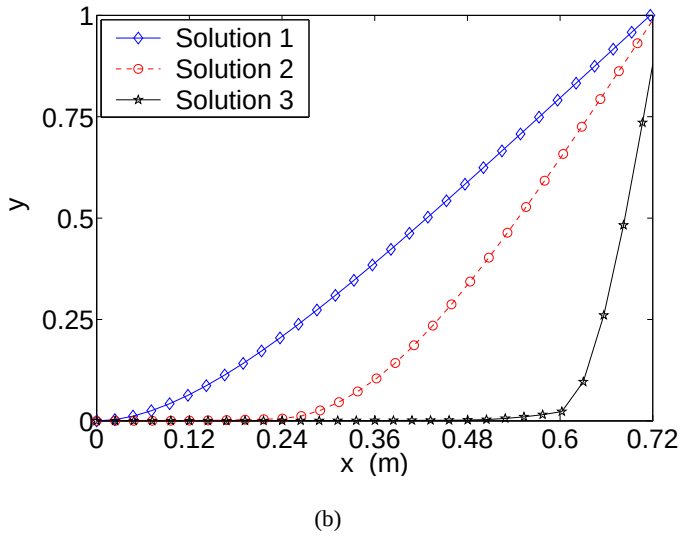

(b)

Fig. 12 Normalized identified thickness distributions for first natural frequency formulation (a) and corresponding modes, normalized by the maximal vertical displacement (b).

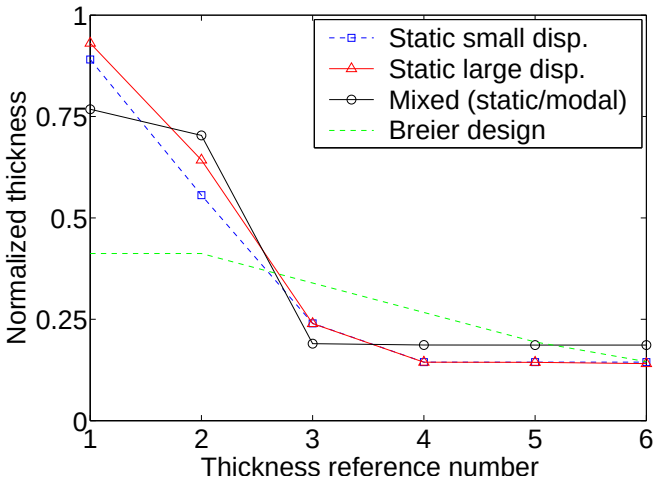

Fig. 13 Comparison among the three identification formulations and the Breier's monofin design.

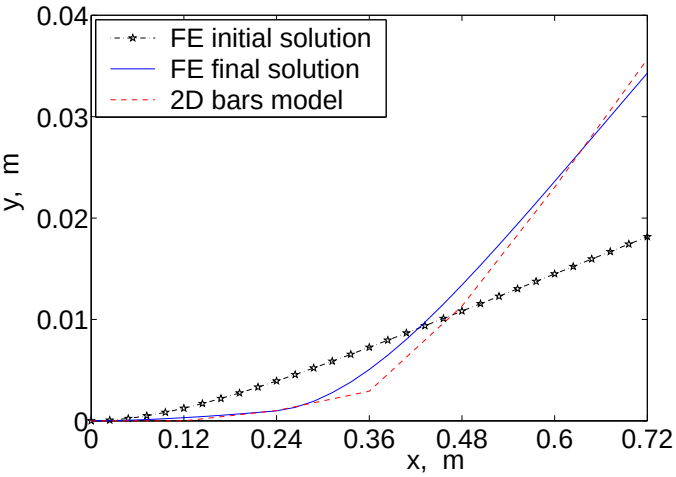

Fig. 14 Deformed shapes comparison for mixed formulation, load case 1.

ping of the result into a three-dimensional structure. The two-dimensional model consists of an unsteady vortex based fluid model in dynamic equilibrium with a bar system representing the fin. It is numerically efficient and can be included into an optimization loop. The flexural distribution over the bar system is optimized by maximizing the propulsive power with a bound on the total power. The optimal stiffness distributions are tapered from the leading to the trailing edge.

The solution has then been translated into a 3D monofin structure. The shape and the material of the monofin are fixed by manufacturing constraints. The thickness distribution is identified to be statically and/or dynamically equivalent to the optimized 2D system. The influence of the various formulations on the final thickness distributions have been studied.

It is recommended to choose the mixed static/dynamic formulation when translating a 2D fin design into 3D. Indeed, the static and dynamic formulations do no yield the same designs. In terms of static analysis, a small displacements finite element model is sufficient. It is observed that small and large displacements formulations do not present significant design differences. Moreover, when mixed formulation is considered, a highly accurate static analysis is not essential because static and dynamic equivalences be-

tween the 2D and 3D models are traded-off, so that there is no longer a precise deformed shapes match.

In both the optimization and identification steps, the GBNM algorithm has performed the minimizations.

Acknowledgements Fundings for this work were provided by CNPq Brazilian research agency for M. A. Luersen and by the Breier fin company, France.

References

Anderson J, Streitlien K, Barret D, Triantafyllou M (1998) Oscillating foils of high propulsive efficiency. Journal of Fluids Mechanics 360:41–72

Baly L, Durey A, Favier D (2001) Etude des fréquences et amplitudes ondulatoires chez le nageur avec palmes de haut niveau. Journées de l'Ecole Doctorale des Sciences de la Vie et de la Santé, Univ de Méditerranée, France URL http://www.ujf-grenoble.fr/ufraps/acaps/Actes/Poster/baly.pdf

Géradin M, Cardona A (2001) Flexible Multibody Dynamics: A Finite Element Approach. John Wiley & Sons, Inc. New York, USA

Kvamsdal T, Jenssen C, Okstad K, Amundsen J (1999) Fluid-structure interaction for structural design. In T Kvamsdal et al, editors, Proc Int Symp on Comput Methods for Fluid-Structure Interaction (FSI'99), Tapir Publishers, Trondheim, Norway pp 211–238

Le Maître O, Huberson S, Souza de Cursi E (1999) Unsteady model of sail and flow interaction. Journal of Fluids and Structures 13:37–59

Lemosse D, Dhatt G (2000) Study of shell-like structures by brick finite element model. In: Proceedings of the Fifth International Conference on Computational Structures Technology, Leuven, Belgium, vol H, pp 183–190

Luersen M, Le Riche R, Le Maître O, Breier E (2003) Optimisation de monopalmes de nage. In: Proceedings of the 6th Colloque National en Calcul des Structures, Giens, France, vol 3, pp 207–214

Luersen M, Le Riche R, Guyon F (2004) A constrained, globalized, and bounded nelder-mead method for engineering optimization. Structural and Multidisciplinary Optimization 27:43–54

Nelder J, Mead R (1965) A simplex for function minimization. Computer Journal 7:308–313

Pedro G, Suleman A, Djilali N (2003) A numerical study of propulsive efficiency of flapping hydrofoil. International Journal for Numerical Methods in Fluids 42:493–526

di Prampero P, Pendergast D, Wilson D, Rennie D (1974) Energetics of swimming in man. Journal of Applied Physiology 37(1):1–5

Sfakiotakis M, Lane D, Davies B (1999) Review of fish swimming modes for aquatic locomotion. IEEE Journal of Oceanic Engineering 24(2):237–252

Zamparo P, Pendergast D, Termin B, Minetti A (2002) How fins affect the economy and efficiency of human swimming. The Journal of Experimental Biology 205:2665–2676

A Flexural stiffness identifiability

When choosing the load cases under which J_{static} is calculated (Eq. (7)), care should be taken to guarantee that the optima are locally unique (local identifiability property). In this regard, it is convenient and sufficiently descriptive to study under which conditions on the loads F_i the 2D bars system of Fig. 15 has a unique set of stiffnesses C_i associated to an equilibrium position θ_i^*, $i = 1, n$.

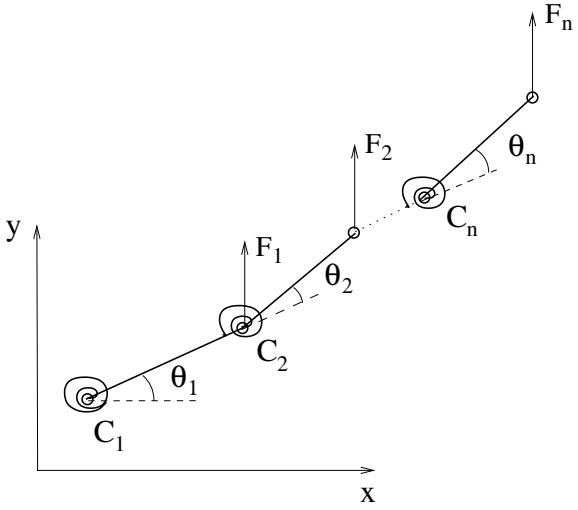

Fig. 15 2D bars system. All bars have lenght l, C_i is the stiffness of the i-th joint, the loads F_i are vertical.

The equilibrium equations of the system are,

$$\begin{cases} C_1\theta_1 = lF_1\cos\theta_1 + lF_2(\cos\theta_1 + \cos(\theta_1+\theta_2)) + \cdots + \\ \qquad + lF_n(\cos\theta_1 + \cdots + \cos(\theta_1+\cdots+\theta_n)) \\ \quad \ldots \\ C_n\theta_n = lF_n\cos(\theta_1+\cdots+\theta_n)\ , \end{cases} \tag{9}$$

or,

$$h_i(\theta_1,\ldots,\theta_n) = 0\ , \quad i = 1, n\ . \tag{10}$$

Let θ_i^*, $i = 1, n$, satisfy the equilibrium equations (10). To see how a change in C_i's affects the equilibrium of the system, a first order approximation to the h_i's is written at θ^*,

$$\left[\frac{\partial h}{\partial C}(\theta^*)\right]\Delta C = 0\ , \tag{11}$$

where components of the Jacobian matrix are, in general,

$$\left[\frac{\partial h}{\partial C}(\theta^*)\right]_{ij} = \frac{\partial h_i}{\partial C_j}(\theta^*) = \frac{dh_i}{dC_j}(\theta^*) + \sum_{k=1}^{n}\frac{\partial h_i}{\partial \theta_k}(\theta^*)\frac{\partial \theta_k}{\partial C_j}(\theta^*)\ . \tag{12}$$

Cases of interest are the problematic ones where, around θ_i^*, a change in C_i's induces no change in the equilibrium, i.e., cases where there are an infinite number of C_i's associated to the same deflected shape θ^* (same J_{static}). At such non-identifiable points, by definition,

$$\frac{\partial \theta_k}{\partial C_j}(\theta^*) = 0 \tag{13}$$

and the Jacobian has null eigenvalues whose associated eigenvectors (stiffness change ΔC) induce no variation of the equilibrium. When (13) holds,

$$\left[\frac{\partial h}{\partial C}(\theta^*)\right]_{ij} = \frac{\partial h_i}{\partial C_j}(\theta^*) = \theta_i^*\delta_{ij}\ , \tag{14}$$

where $\delta_{ij} = 1$ if $i = j$; $\delta_{ij} = 0$ otherwise.

This establishes that the Jacobian eigenvalues are the equilibrium angles. Local non-identifiability occurs when some of the equilibrium angles are null, which is intuitive since the associated springs have no action. Two typical scenarii where some θ_i^* are null are depicted in

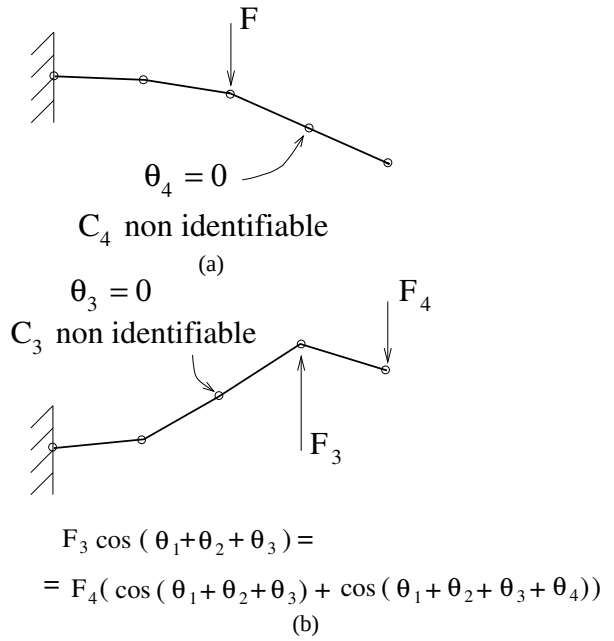

Fig. 16 Examples of loads such that the flexural stiffnesses are not identifiable, (a) the tip is not loaded, (b) moments cancel at joint 3.

Fig. 16, first when the tip of the system is not loaded, then when the moments cancel at a joint.

Besides the load case, we note, without formal proof, that the control points used to calculate J_{static} should be numerous and well spread on the system in order to guarantee the uniqueness of $\arg\min_{C \text{ or } h} J_{static}$. As a counter-example (see Fig. 17), if there is only a control point at the tip with a target displacement (u^t, v^t), it should be clear that there is an infinite number of choices of $(C_1^*, \ldots, C_n^*, \theta_1^*, \ldots, \theta_n^*)$ such that

$$\begin{cases} \text{(10) is satisfied and} \\ l(\cos\theta_1^* + \cdots + \cos(\theta_1^* + \cdots + \theta_n^*)) = u^t \\ l(\sin\theta_1^* + \cdots + \sin(\theta_1^* + \cdots + \theta_n^*)) = v^t \end{cases} \tag{15}$$

because (15) is a system of $(n+2)$ equations in $2n$ unknowns.

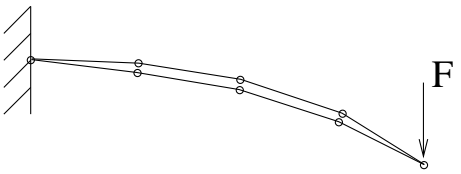

Fig. 17 Two deflected shapes that have the same displacements at the tip. This illustrates why C_i's would not be identifiable if there was only a control point at the tip.